Oxygen Reduction on $LaMnO_3$-Based Cathode Materials in Solid Oxide Fuel Cells

YongMan Choi,[†] David S. Mebane,[†] M. C. Lin,[‡,§] and Meilin Liu*[,†]

Center for Innovative Fuel Cell and Battery Technologies, School of Materials Science and Engineering, Georgia Institute of Technology, Atlanta, Georgia 30332, Department of Chemistry, Emory University, 1515 Dickey Drive, Atlanta, Georgia 30322, and Center for Interdisciplinary Molecular Science, National Chiao Tung University, Hsinchu, 30010, Taiwan

Received November 1, 2006. Revised Manuscript Received January 29, 2007

Cubic perovskite $LaMnO_3$ surface models were constructed to elucidate the mechanism of oxygen reduction using quantum chemical calculations with molecular dynamics (MD) simulations. Calculations predict that both dissociative and molecular adsorption may occur, depending on adsorbate configurations. Superoxo- or peroxo-like species may locate at La, Mn, and O_{sub} active sites with different vibrational frequencies and atomic charges. A stepwise elementary reaction sequence via the superoxo- or peroxo-like intermediates at both perfect and defective $LaMnO_3$ was constructed by mapping out minimum-energy paths (MEPs) using the nudged elastic band (NEB) method. Charge transfer for the $O_2-LaMnO_3$ interactions was also explored by Bader charge analysis. In particular, ab initio MD simulations carried out to simulate solid oxide fuel cell conditions at 1073 K suggest that oxygen vacancies enhance O_2 dissociation kinetics.

1. Introduction

Solid oxide fuel cells (SOFCs) have attracted much attention because of their high-energy efficiency and excellent fuel flexibility.[1−8] While the development of SOFC technology has moved forward rapidly in recent years, understanding the detailed mechanisms of interfacial reactions remains a grand challenge.

The overall electrochemical reaction for oxygen reduction at the cathode of an SOFC can be generally described as follows:

$$^1/_2O_2(g) + 2e^- \rightarrow O^{2-} \quad (1)$$

However, the detailed mechanism of oxygen reduction can be very complicated. According to a phenomenological description[9,10] for the oxygen reduction reaction at the interface of porous cathode/electrolyte composite materials under SOFC operating conditions, oxygen first adsorbs at the cathode surface with either an end- or a side-on intermediate. Then, the adsorbed oxygen species directly dissociates to monatomic oxygen ions (O^-) or is reduced to diatomic superoxo- and peroxo-like species (O_2^- and O_2^{2-}, respectively), followed by dissociation to monatomic oxygen ions. Subsequently, the dissociated oxygen ions either reduce to O^{2-} followed by incorporation into the lattice or combine directly with an electron and an oxygen vacancy. Furthermore, surface diffusion of the oxygen species may occur, and then the adsorbed oxygen species may move to or near triple-phase boundaries (TPBs), where a cathode, an electrolyte, and oxygen species meet at electrochemically active sites. Although numerous extensive studies[11−15] for the oxygen reduction reaction at SOFC cathode materials have been performed, the mechanism has not been fully understood as a result of the complexity of the interfacial phenomena at or near TPBs. Impedance spectroscopy (IS) has been widely applied to characterize electrochemical performance in SOFCs, but it has provided limited information about the reaction mechanism so far.[16] Although preliminary studies of the oxygen reduction reaction using in situ vibrational surface spectroscopy[17−19] have been

* Corresponding author. Tel.: +1-404-894-6114. Fax: +1-404.894.9140. E-mail: meilin.liu@mse.gatech.edu.
[†] Georgia Institute of Technology.
[‡] Emory University.
[§] National Chiao Tung University.

(1) Minh, N. Q. *J. Am. Ceram. Soc.* **1993**, *76*, 563.
(2) Minh, N. Q. *Solid State Ionics* **2004**, *174*, 271.
(3) Minh, N. Q.; Takahashi, T. *Science and Technology of Ceramic Fuel Cells*; Elsevier: Amsterdam, 1995.
(4) Singh, P.; Minh, N. Q. *Int. J. Appl. Ceram. Technol.* **2004**, *1*, 5.
(5) Singhal, S. C. *Solid State Ionics* **2000**, *135*, 305.
(6) Singhal, S. C. *Solid State Ionics* **2002**, *152−153*, 405.
(7) Singhal, S. C.; Kendall, K. *High-temperature Solid Oxide Fuel Cells: Fundamentals, Design and Applications*; Elsevier Science: New York, 2003.
(8) Steele, B. C. H.; Heinzel, A. *Nature* **2001**, *414*, 345.
(9) Pizzini, S. General aspects of kinetics of ion-transfer across interfaces. In *Fast Ion Transport in Solids*; van Gool, W., Ed.; North-Holland: Amsterdam, 1973; p 461.
(10) Steele, B. C. H. *Solid State Ionics* **1996**, *86−88*, 1223.
(11) Adler, S. B. *Solid State Ionics* **1998**, *111*, 125.
(12) Deng, H.; Zhou, M.; Abeles, B. *Solid State Ionics* **1995**, *80*, 213.
(13) Svensson, A. M.; Nisancioglu, K. *J. Electrochem. Soc.* **1998**, *145*, 3130.
(14) Svensson, A. M.; Sunde, S.; Nisancioglu, K. *J. Electrochem. Soc.* **1998**, *145*, 1390.
(15) Kuo, J. H.; Anderson, H. U.; Sparlin, D. M. *J. Solid State Chem.* **1989**, *83*, 52.
(16) Xia, C.; Liu, M. *Adv. Mater.* **2002**, *14*, 521.
(17) Liu, M.; Lu, X.; Faguy, P. In situ characterization of electrode reactions in solid oxide fuel cells. *Proceedings of Solid Oxide Fuel Cells VIII*; The Electrochemical Society: Pennington, NJ, 2003; p 1132.
(18) Lu, X.; Faguy, P. W.; Liu, M. *Proceedings of Solid-State Ionic Devices III*; The Electrochemical Society: Pennington, NJ, 2003; p 340.
(19) Lu, X.; Faguy, P. W.; Liu, M. *J. Electrochem. Soc.* **2002**, *149*, A1293.

10.1021/cm062616e CCC: $37.00
Published on Web 03/10/2007

conducted, mechanistic details have not been directly observed experimentally.[20] Furthermore, experimental studies to date are still unable to identify the active sites for the oxygen reduction reaction at the SOFC cathodes.[21] Quantum chemical calculations[22−27] may be a powerful approach to elucidate the O_2−cathode interactions as the technique can provide electronic structures, geometrical parameters, and energetics of bulk and adsorbed intermediate species. Owing to rapid advances in computation and theoretical methodology, numerous theoretical studies on the most widely used $LaMnO_3$ cathode material have been reported.[28−43] However, to the best of our knowledge, no detailed mechanistic studies of the oxygen reduction at the $LaMnO_3$-based cathode materials using quantum chemical calculations are available in the literature. Here we report our results on the application of periodic density functional theory (DFT) calculations to exploration of the molecular processes involved in oxygen reduction on perfect and defective $LaMnO_3$ surfaces, predicting the most probable oxygen reaction pathway as well as the vibrational frequencies and atomic charges of the adsorbed surface oxygen species.

2. Computational Details

Similar to our previous study of the O_2−CeO_2 interactions,[20] as implemented in the Vienna ab initio simulation package (VASP),[44,45] the periodic DFT method with the projector augmented wave (PAW)[46] method was applied. For the exchange and correlation energies, we used the generalized gradient approximation (GGA) with the Perdew−Wang (PW91) functional.[47] In this study, we consider only the highly symmetric cubic perovskite structure of *Pm*3*m* since the $LaMnO_3$ cathode material has a cubic structure under SOFC operating conditions.[28−30] On the basis of a detailed study by Kotomin and co-workers,[33] all calculations were carried out using ($4 \times 4 \times 4$) Monkhorst−Pack mesh[48] *k*-points and with a 400 eV cutoff energy, allowing convergence to 0.01 eV of the total electronic energy. Convergence criteria for the ionic update cycle and the electronic self-consistency cycle were set to 10^{-4} and 10^{-5} eV/atom, respectively. We chose the spin-polarized method to properly describe the magnetic property of $LaMnO_3$ and the triplet ground state of oxygen. Regarding our initial calculations for ferromagnetic (FM) and anti-ferromagnetic (AFM) states of $LaMnO_3$, the FM configuration is ∼0.5 eV more stable than the AFM configuration, proving the ground state of the cubic $LaMnO_3$ phase is FM. This is similar to the previous work by Evarestov and co-workers.[30] In particular, the adsorption energy difference for the interaction of a superoxo-like species with the FM and AFM states is less than 0.03 eV, which is within the uncertainty of DFT methods (∼0.09 eV).[49] Thus, all the calculations were carried out based on the FM state. The estimated bulk lattice constant for $LaMnO_3$ is 3.876 Å, which is in good agreement with the experimental values of 3.879 Å[50] and 3.889 Å[51] (see Figure 1). After optimizing various intermediate states, vibrational frequencies of adsorbed oxygen species were calculated to identify their superoxo- or peroxo-like characteristics, providing a scientific basis for direct identification of these species at cathode surfaces using surface vibrational spectroscopy. For the calculations, the surface was fixed, while only adsorbed oxygen species were displaced. The nudged elastic band (NEB) method[52,53] was used to map out minimum-energy paths (MEPs) by connecting reactants, local minima, or products. Atomic charges of the optimized structures were estimated to examine charge transfer between the adsorbates and the substrate by means of the Bader analysis program,[54,55] which is based on Bader's theory of atoms in molecules (AIM) regarding the topological properties of electronic densities of molecules.[56,57] Furthermore,

(20) Choi, Y. M.; Abernathy, H.; Chen, H.-T.; Lin, M. C.; Liu, M. *ChemPhysChem* **2006**, *7*, 1957.
(21) It has been reported that the B cations of the perovskite ABO_3 cathode materials such as Sr-doped $LaMnO_3$, $LaFeO_3$, $LaCoO_3$, and $LaCrO_3$ play a pivotal role in the catalytic activity for the oxygen reduction. Therefore, we may need to characterize the B cation site for the defective surfaces using the cathode materials.
(22) Hermse, C. G. M.; van Bavel, A. P.; Koper, M. T. M.; Lukkien, J. J.; van Santen, R. A.; Jansen, A. P. J. *Surf. Sci.* **2004**, *572*, 247.
(23) Jacobsen, C. J. H.; Dahl, S.; Clausen, B. S.; Bahn, S.; Logadottir, A.; Norskov, J. K. *J. Am. Chem. Soc.* **2001**, *123*, 8404.
(24) Linic, S.; Barteau, M. A. *J. Am. Chem. Soc.* **2004**, *126*, 8086.
(25) Linic, S.; Jankowiak, J.; Barteau, M. A. *J. Catal.* **2004**, *224*, 489.
(26) Neurock, M. *J. Catal.* **2003**, *216*, 73.
(27) Strasser, P.; Fan, Q.; Devenney, M.; Weinberg, W. H.; Liu, P.; Norskov, J. K. *J. Phys. Chem. B* **2003**, *107*, 11013.
(28) Evarestov, R. A.; Kotomin, E. A.; Fuks, D.; Felsteiner, J.; Maier, J. *Appl. Surf. Sci.* **2004**, *238*, 457.
(29) Evarestov, R. A.; Kotomin, E. A.; Heifets, E.; Maier, J.; Borstel, G. *Solid State Commun.* **2003**, *127*, 367.
(30) Evarestov, R. A.; Kotomin, E. A.; Mastrikov, Y. A.; Gryaznov, D.; Heifets, E.; Maier, J. *Phys. Rev. B* **2005**, *72*, 214411/1.
(31) Fuks, D.; Bakaleinikov, L.; Kotomin, E. A.; Felsteiner, J.; Gordon, A.; Evarestov, R. A.; Gryaznov, D.; Maier, J. *Solid State Ionics* **2006**, *177*, 217.
(32) Fuks, D.; Dorfman, S.; Felsteiner, J.; Bakaleinikov, L.; Gordon, A.; Kotomin, E. A. *Solid State Ionics* **2004**, *173*, 107.
(33) Kotomin, E. A.; Evarestov, R. A.; Mastrikov, Y. A.; Maier, J. *Phys. Chem. Chem. Phys.* **2005**, *7*, 2346.
(34) Kotomin, E. A.; Heifets, E.; Dorfman, S.; Fuks, D.; Gordon, A.; Maier, J. *Surf. Sci.* **2004**, *566*−*568*, 231.
(35) Kotomin, E. A.; Heifets, E.; Maier, J.; Goddard, W. A., III. *Phys. Chem. Chem. Phys.* **2003**, *5*, 4180.
(36) Woodley, S. M.; Catlow, C. R. A.; Gale, J. D.; Battle, P. D. *Chem. Commun.* **2000**, 1879.
(37) Su, Y. S.; Kaplan, T. A.; Mahanti, S. D.; Harrison, J. F. *Phys. Rev. B* **2000**, *61*, 1324.
(38) Islam, M. S. *J. Mater. Chem.* **2000**, *10*, 1027.
(39) Islam, M. S. *Solid State Ionics* **2002**, *154*−*155*, 75.
(40) Kovaleva, N. N.; Gavartin, J. L.; Shluger, A. L.; Boris, A. V.; Stoneham, A. M. *J. Exp. Theor. Phys.* **2002**, *94*, 178.
(41) Ravindran, P.; Kjekshus, A.; Fjellvag, H.; Delin, A.; Eriksson, O. *Phys. Rev. B* **2002**, *65*, 064445/1.
(42) Nicastro, M.; Patterson, C. H. *Phys. Rev. B* **2002**, *65*, 205111.
(43) Munoz, D.; Harrison, N. M.; Illas, F. *Phys. Rev. B* **2004**, *69*, 085115/1.
(44) Kresse, G.; Furthmüller, J. *Phys. Rev. B* **1996**, *54*, 11169.
(45) Kresse, G.; Hafner, J. *Phys. Rev. B* **1993**, *47*, 558.
(46) Blöchl, P. *Phys. Rev. B* **1994**, *17*, 953.
(47) Perdew, J. P.; Burke, K.; Ernzerhof, M. *Phys. Rev. Lett.* **1996**, *77*, 3865.
(48) Monkhorst, H. J.; Pack, J. D. *Phys. Rev. B* **1976**, *13*, 5188.
(49) Kohn, W.; Becke, A. D.; Parr, R. G. *J. Phys. Chem.* **1996**, *100*, 12974.
(50) Jena, H.; Govindan, Kutty, K. V.; Kutty, T. R. N. *J. Alloys Compd.* **2003**, *350*, 102.
(51) Arima, T.; Tokura, Y. *J. Phys. Soc. Jpn.* **1995**, *64*, 2488.
(52) Henkelman, G.; Uberuaga, B. P.; Jönsson, H. *J. Chem. Phys.* **2000**, *113*, 9901.
(53) Mills, G.; Jönsson, H.; Schenter, G. *Surf. Sci.* **1995**, *324*, 305.
(54) Henkelman, G.; Arnaldsson, A.; Jönsson, H. *Comput. Mater. Sci.* **2006**, *36*, 354.
(55) http://theory.cm.utexas.edu/bader/(accessed Oct. 2006).
(56) Bader, R. F. W.; Beddall, P. M. *J. Chem. Phys.* **1972**, *56*, 3320.
(57) Bader, R. F. W. *Atoms in Molecules - A Quantum Theory*; Clarendon Press: Oxford, 1994.

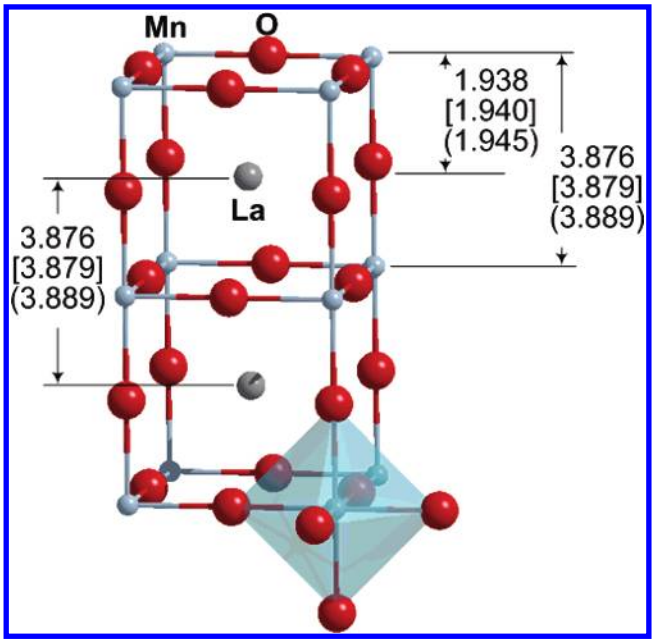

Figure 1. Bulk structure of cubic perovskite $LaMnO_3$. The values in the brackets and the parentheses represent the experimental data from refs 50 and 51, respectively.

Table 1. Summary of Calculated Surface Energies of $LaMnO_3$(111), (110), and (100)

	surface energies (J/m^2)		
	(100)	(110)	(111)
unrelaxed	1.60	2.68	1.86
relaxed	0.83	1.37	1.37
S^a ($\times 10^{-19}$, m^2)	3.01	4.25	5.21

[a] Surface area.

we carried out molecular dynamics (MD) calculations using the VASP code to simulate SOFC operating conditions at 1073 K.

3. Results and Discussion

A. Characterization of Bulk $LaMnO_3$ and Low-Index $LaMnO_3$(111), (110), and (100). To examine the surface stability of low-index (111), (110), and (100) surfaces, we constructed surface models as periodically repeated slabs consisting of six, eight, and six atomic layers, respectively, as illustrated in Figure 1 and Figure S1 (Supporting Information). Slabs of the surfaces were separated by a vacuum space that is 2.5 times as thick as each slab. Summarized in Table 1 are the surface energies in the units of J/m^2 of $LaMnO_3$-(111), (110), and (100) as estimated according to the equation $E_{surf} = \frac{1}{2S}(E_{slab} - E_{bulk})$, where E_{surf}, S, E_{slab}, and E_{bulk} correspond to the surface energy, the surface area, and the calculated electronic energies of the slab and the bulk, respectively.[58] It is found that the (100) surface may be energetically the most stable among the surface models (see Table 1), which is in line with the previous study.[30] In this study, however, we chose the (110) surface with LaMnO- and O-terminated layers to examine oxygen reduction at both La and Mn cations because the (100) surface is terminated by a LaO or MnO layer. To examine the JT effects on splitting of Mn 3d levels into t_{2g}- and e_g-like levels[41,59] we have calculated the local density of states for Mn ions on the (110) surface model used for oxygen reduction. As shown in Figure S2 (Supporting Information), these levels are nearly overlapped, implying that the JT effects for the oxygen reduction reaction are insignificant. To conserve computational resources, the surface size for surface calculations was reduced as shown in Figures 2b and 2c. We found that relaxing the three top layers may be sufficient to carry out surface calculations. Therefore, in this study, all the surface calculations for $O_2-LaMnO_3$ interactions were carried out on the LaMnO- and O-terminated $LaMnO_3$(110) surface models by relaxing the three top layers. In addition, based on the approach by Jiang and co-workers,[60] the O-vacancy formation energy of $LaMnO_3$ ($LaMnO_3 \rightarrow LaMnO_{3-x} + V_O^{\bullet\bullet} + {}^1/_2O_2(g)$) was calculated as $E_{O-vac} = E[LaMnO_{3-x}] + {}^1/_2E[O_2] - E[LaMnO_3]$, where $LaMnO_{3-x}$ and $V_O^{\bullet\bullet}$ represent defective $LaMnO_3$ and an oxygen vacancy, respectively. $E[LaMnO_{3-x}]$ and $E[LaMnO_3]$ denote the calculated electronic energies of defective and perfect $LaMnO_3$ surfaces, respectively. $E[O_2]$ is the predicted energy of triplet O_2 in a 10 Å cubic box[20] (see Table S1, Supporting Information). In this study, the theory at the GGA−PAW−DFT level predicts E_{O-vac} of approximately 4.85 eV.

B. Surface Oxygen Intermediates on $LaMnO_3$(110). In this study, the adsorption energy is defined as $\Delta E_{ads} = E_P - E_R$, where E_P and E_R are the calculated electronic energies of bonded and nonbonded oxygen species on $LaMnO_3$, respectively.

It is well-known that surface adsorption processes are affected by surface active sites.[20,61] Thus, we initially studied dissociative and molecular adsorption of $O_2-LaMnO_3$(110) interactions. As illustrated in Figures 2b and 2c plausible intermediates were optimized by placing an oxygen molecule at various active sites on LaMnO- and O-terminated surfaces, including "La-top", "Mn-top", "O-top", "O_{sub}-top", and "O-top" corresponding to **La-I**, **Mn-I**, **O-I**, **O-II**, and **O-I**, respectively.

Various configurations of adsorbed oxygen species for molecular adsorption were located, corresponding to end-on, side-on, or bridging structures. The intermediates were categorized based on the notation of **a**, **b**, **c**, and **d** (see Figure 2). **v** of **Mn-a-v** denotes a vertically adsorbed structure, **V** of **Mn-a-V** represents an intermediate optimized on defective $LaMnO_3$, and **sub** of **O-sub** means the second layer on the surface model. Figure 3 illustrates the optimized geometries of adsorbed di-oxygen and dissociated monatomic species. Table 2 summarizes adsorption energies ($-3.54 < \Delta E_{ads} < -0.40$ eV). The energies listed in Table 2 clearly show that the LaMnO-terminated surface is energetically more favorable for oxygen reduction than the O-terminated surface. As compiled in Tables 2 and 3, atomic charges of adsorbed di-

(58) Yang, Z.; Woo, T. K.; Baudin, M.; Hermansson, K. *J. Chem. Phys.* **2004**, *120*, 7741.
(59) Satpathy, S.; Popović, Z. S.; Vukajlović, F. R. *Phys. Rev. Lett.* **1996**, *76*, 960.
(60) Jiang, Y.; Adams, J. B.; Schilfgaarde, M. V. *J. Chem. Phys.* **2005**, *123*, 064701.
(61) Pushkarev, V. V.; Kovalchuk, V. I.; d'Itri, J. L. *J. Phys. Chem. B* **2004**, *108*, 5341.

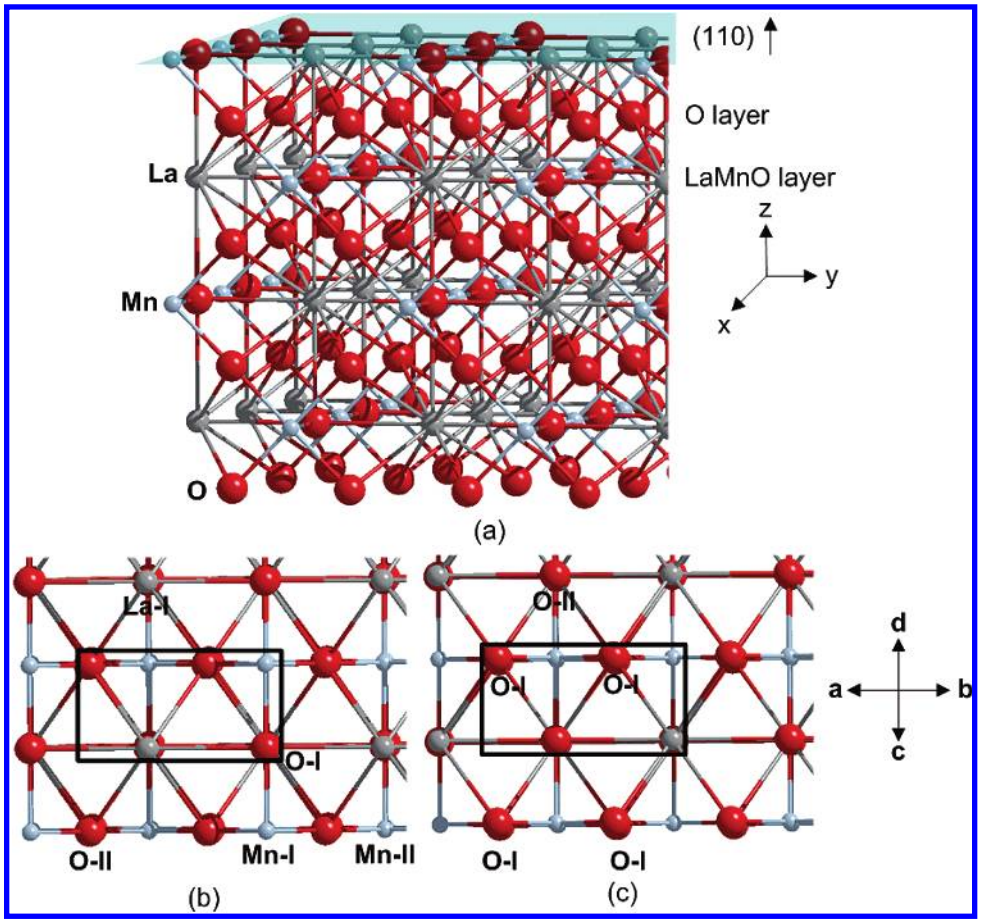

Figure 2. (a) Side view of LaMnO-terminated $LaMnO_3$ (110). (b and c) Top views of LaMnO- and O-terminated $LaMnO_3$ (110) surfaces, respectively. The rectangles represent the supercell cells for surface calculations. **I** and **II** correspond to the atoms on the top and second layers, respectively.

and monatomic oxygen species were estimated by Bader charge analysis.[54,55] The Bader charge analysis shows that charge transfers from the surface, especially La, Mn, and O ions on the top layer, to adsorbed oxygen species. Also, it clearly shows that the contribution of the sublayers to charge transfer is insignificant during adsorption and dissociation. As shown in Tables 2 and 3, the atomic charges of the dissociated oxygen monatomic species are close to that of the oxygen anions of the substrate (see Table S2, Supporting Information).

In addition to the perfect $LaMnO_3$ surface model, a defective surface was generated by removing an oxygen anion (O^{2-}), **O-I**, from the top layer, as shown in Figure 2b. The defective model is more representative of the actual SOFC cathode materials such as Sr-doped $LaMnO_3$.[62] As summarized in Table 3 and Figure 4, the optimized geometries of the adsorbed oxygen species on the defective $LaMnO_3$ are slightly different from those on the perfect surface. Table 3 lists the altered O−O bonds and their vibrational frequencies. Those intermediates on the defective $LaMnO_3$ surface are energetically more favorable and have different atomic charges compared to those on the perfect surface. Regarding the atomic charges, those intermediates optimized at the defective surfaces are noticeably changed (see Table S4, Supporting Information), whereas those of the bulk and the perfect surfaces are very close. In particular, we categorized intermediates as superoxo- or peroxo-like species based on the predicted geometry and vibrational frequency (see Tables 2 and 3).

Similar to the manner in which we compared the coverage effect on the H_2S−Ni interactions using different surfaces,[63] a double-sized $LaMnO_3$ surface was constructed, and the **Mn-c-d** configuration was applied. Interestingly, the adsorption energy difference of the peroxo-like species is insignificant, with a slight change in the bond distance and vibrational frequency (from 1.420 to 1.431 Å and from 975 to 949 cm^{-1}, respectively). This means that our initial surface size may be sufficient for characterizing the oxygen reduction reaction on the $LaMnO_3$ surface models.[62]

C. Reaction Mechanisms of Oxygen Reduction on LaMnO-Terminated $LaMnO_3$(110). As mentioned, we constructed the MEPs using the NEB method on the LaMnO-terminated surface to theoretically characterize the oxygen reduction reaction on $LaMnO_3$ surfaces. As a result of the absence of the **O-sub** intermediate on the defective surface, as shown in Table 3, only the reaction pathways based on local minima adsorbed on A and B cations (La and Mn, respectively) were examined to properly compare the reaction mechanisms on the perfect surfaces with those on the defective surfaces. Figures 5 and 6 display the potential

(62) $La_{1-x}Sr_xMnO_3$ (x = 0.17 and 0.5) surface models have been constructed, and more realistic mechanistic results will be reported in a future article.

(63) Choi, Y. M.; Compson, C.; Lin, M. C.; Liu, M. *Chem. Phys. Lett.* **2006**, *421*, 179.

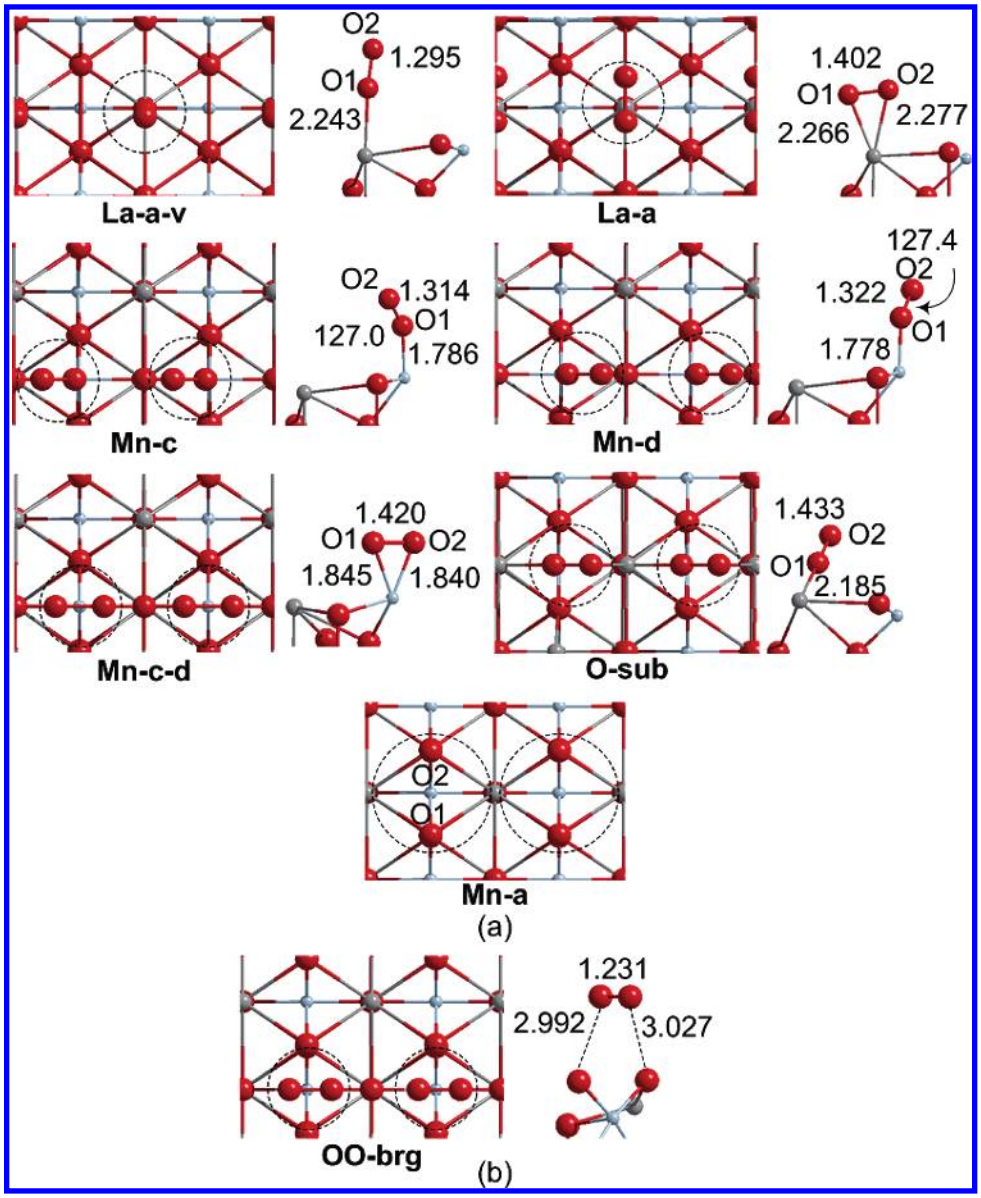

Figure 3. Optimized geometries for the oxygen reduction reaction on (a) LaMnO- and (b) O-terminated $LaMnO_3$ (110). The bond lengths are in Å. Dashed circles represent adsorbed oxygen species on the surface.

Table 2. Adsorption Energies, Geometrical Parameters, Predicted Vibrational Frequencies, and Atomic Charges of Adsorbed Oxygen Species on the Perfect $LaMnO_3$(110) Surfaces

species	adsorption energy[a] (eV)	r(O−O) (Å)	υ_{OO} (cm^{-1})	atomic charge (e) O1	O2	sum	remark
LaMnO Termination							
$LaMnO_3 + O_2$	0.00						
La-a-v	−1.51	1.302	1207	−0.07	−0.51	−0.58	superoxo-
La-a	−2.35	1.404	979	−0.41	−0.48	−0.90	peroxo-
Mn-c	−1.76	1.314	1177	−0.47	−0.20	−0.67	superoxo-
Mn-d	−1.80	1.322	1143	−0.44	−0.24	−0.68	superoxo-
Mn-c-d	−2.20	1.420	975	−0.56	−0.41	−0.97	peroxo-
O-sub	−3.54	1.433	957	−0.44	−0.73	−1.17	peroxo-
Mn-a	−7.36	-	-	−1.08	−1.06	−2.14	dissociated product[a]
O Termination							
$LaMnO_3 + O_2$	0.00						
OO-brg	−0.40	1.232	1558	0.07	−0.18	−0.11	physi-sorption

[a] **Mn-a** corresponds to the final product in the mechanistic study.

Table 3. Adsorption Energies, Geometrical Parameters, Predicted Vibrational Frequencies, Atomic Charges of Adsorbed Oxygen Species on the LaMnO-Terminated Defective $LaMnO_3$(110) Surface

species	adsorption energy (eV)	r(O−O) (Å)	υ_{OO} (cm^{-1})	atomic charge (e) **O1**	**O2**	sum	remark
$LaMnO_{3-x} + O_2$	0.00						
La-a-V	−9.31			−1.29	−1.24	−2.53	dissociated
La-a-v-V	−1.12	1.304	1176	−0.49	−0.13	−0.62	superoxo-
Mn-c-V	−1.82	1.301	1265	−0.57	−0.18	−0.75	superoxo-
Mn-c-d-V	−2.70	1.445	861	−0.46	−0.60	−1.06	peroxo-
P-v-V	−6.99			−1.32	−0.92	−2.24	dissociated
products	−9.32			−1.30	−1.23	−2.53	

energy profiles and estimated atomic charges.

On the Perfect $LaMnO_3$ Surface. Figure 5 illustrates molecular adsorption pathways via two active sites of La and Mn cations on the perfect $LaMnO_3$(110) surface. It the asymptotic region (>4.0 Å), the bond length of the oxygen molecule is close to that of the gas phase, ∼1.23 Å (see Table S1, Supporting Information). As the oxygen molecule approaches the La or Mn cations of the substrate, the total energy decreases and forms the superoxo-like **La-a-v** and **Mn-c** intermediates with exothermicities of 1.51 and 1.76 eV, respectively. The process involves elongation of the O−O bond (1.295 and 1.314 Å, respectively) in which the O−O bond is not yet fully cleaved (see Figure 3). After

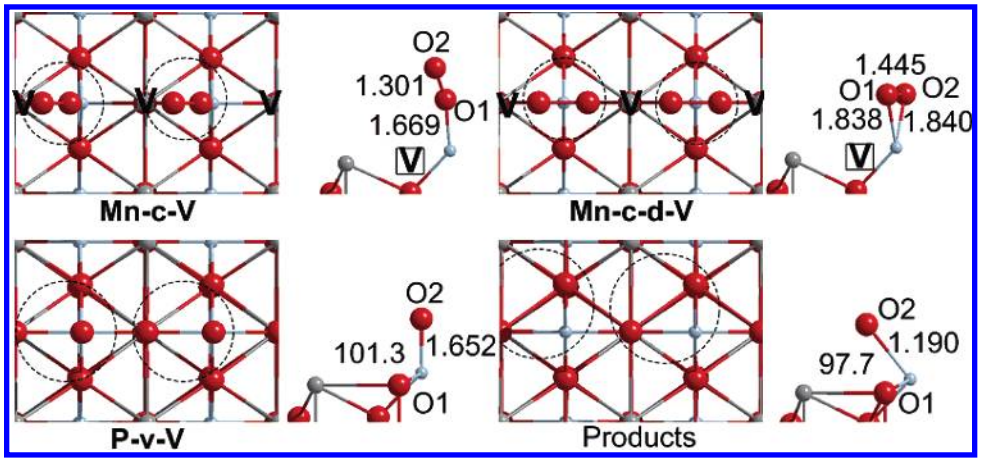

Figure 4. Geometrical parameters for the adsorbed oxygen species on LaMnO-terminated $LaMnO_3$ (110) with an oxygen vacancy. The bond lengths and angles are in Å and deg. **V** and dashed circles represent a doubly charged oxygen vacancy and adsorbed oxygen species on the surface, respectively.

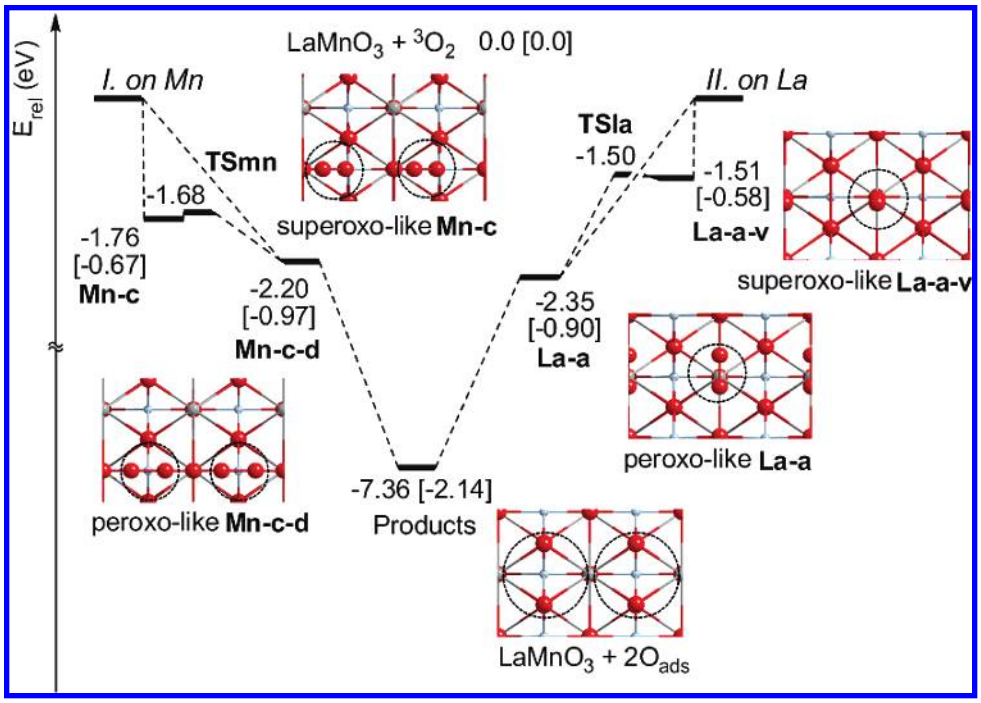

Figure 5. Potential energy profiles at 0 K for the oxygen reduction reaction on the perfect $LaMnO_3$ surface. The values in brackets are the sum of the estimated atomic charges of **O1** and **O2**.

overcoming small reaction barriers of 0.01 and 0.08 eV at **TSla** and **TSmn**, respectively, the superoxo-like intermediates convert to the peroxo-like **La-a** and **Mn-c-d** intermediates along with elongation of the O−O bond distance, whose exothermicities are 2.35 and 2.20 eV, respectively. In addition, it was found that **La-a** and **Mn-c-d** can form directly from the reactants without barrier, which was verified by the NEB calculations. Then, the peroxo-like species dissociates to produce two oxygen atoms with an exothermicity of 7.36 eV, proving that the adsorption/dissociation process on the perfect $LaMnO_2$ surface is energetically favorable. Our extensive NEB calculations show that the process may occur without barrier except for the small reaction barriers for the isomerization process from the superoxo- to peroxo-like species. The atomic-charge calculations of each intermediate and product clearly demonstrate that as the adsorption/dissociation process proceeds via the two active sites (La and Mn sites), the charge becomes more negative.

On the Defective $LaMnO_3$ Surface. Similar to the perfect $LaMnO_3$ surface, we carried out a mechanistic study for the molecular adsorption pathway at the defective $LaMnO_3$ surface as discussed in the previous section. As shown in Figure 4 and Table 3, we failed to locate the peroxo-like species at the La cation site; thus, we considered only the Mn cation pathway. The mechanistic result will be compared with our future study on a $La_{1-x}Sr_xMnO_3$ (LSM) surface.[21,62] As depicted in Figure 6, the first step is the formation of either superoxo-like **Mn-c-V** or peroxo-like **Mn-c-d-V** with exothermicities of 1.82 or 2.70 eV, respectively. As seen in Table 3, they have distinct vibrational frequencies of 1265 and 861 cm^{-1}. Because of the further charge transfer from the surface to the adsorbate, superoxo-like **Mn-c-V** can also isomerize to the peroxo-like **Mn-c-d-V** intermediate after overcoming a 0.1 eV reaction barrier of **TSv**, leading to a lengthening of the O−O bond distance from 1.301 to 1.445 Å (see Figure 4). Comparing the energetics, **Mn-c-V** and **Mn-c-d-V** are more exothermic than those at the perfect

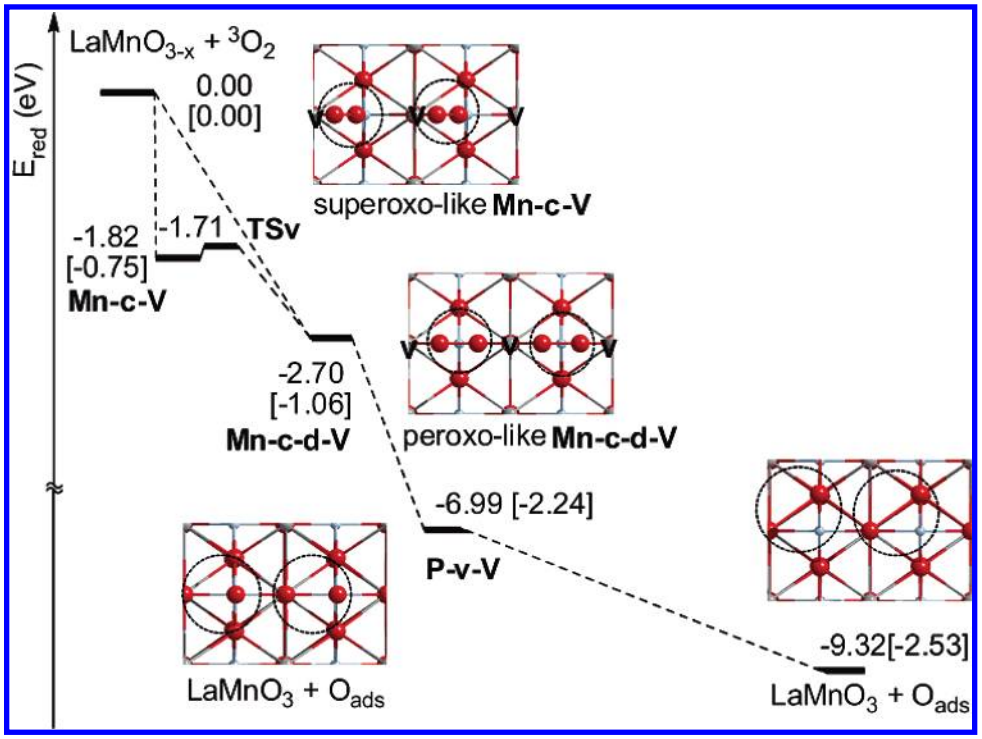

Figure 6. Potential energy profile at 0 K for the oxygen reduction reaction on the defective $LaMnO_3$ surface. The values in brackets are the sums of the estimated atomic charges of **O1** and **O2**.

$LaMnO_3$ surface, suggesting that the adsorption/dissociation process at the defective $LaMnO_3$ surface is energetically more favorable than at perfect $LaMnO_3$. Then, one of the oxygen atoms of the peroxo-like **Mn-c-d-V** species is incorporated into the doubly charged oxygen vacancy ($V_O^{\bullet\bullet}$) while breaking the O−O bond without barrier, producing $LaMnO_3 + O_{ads}$, **P-v-V** with an exothermicity of 6.99 eV. The monatomic oxygen species absorbed at the Mn cation diffuses to a more stable site (labeled as Products in Figure 4), which is 2.32 eV more stable than **P-v-V**.

As compiled in Tables 2 and 3 and Figures 5 and 6, adsorbed di- or monatomic oxygen species become negatively charged, characteristic of a charge transfer from the substrate to the adsorbates. We found that the very presence of an oxygen vacancy influences diffusion at the surface, with the lowest-energy sites occurring in the neighborhood of the vacancy. The sum of atomic charges on the defective surface is more negative than that on the perfect surface, suggesting a greater extent of charge transfer at the defective substrate. On the basis of the quantitative analysis in terms of the energetics and atomic charges, defective $LaMnO_3$ is more favorable for the overall process than perfect $LaMnO_3$.

According to the mechanistic studies, there may be relatively small barriers for isomerization of the superoxo- to peroxo-like intermediate, but there are no barriers for adsorption, incorporation into the bulk, and diffusion on the surface, demonstrating that La-based ABO_3 materials have fast O_2 kinetics. Furthermore, the computed vibrational frequencies for the O−O stretching of peroxo- and superoxo-like oxygen species are 1143−1265 or 861−1017 cm^{-1}, respectively, depending on configurations and computational methods. To the best our knowledge, only one study[64] reported experimental oxygen absorption bands on La-based materials, that is, 802 and 820 cm^{-1}, which may be attributed to peroxo-like species. Thus, we can only qualitatively assign the adsorbed oxygen species due to the lack of experimental data.[65,66] The predicted vibrational frequencies in this study, however, will be verified by surface vibrational spectroscopy similar to O_2-CeO_2 measurements.[20,61]

D. MD Simulations on LaMnO-Terminated $LaMnO_3$-(110). To simulate SOFC conditions on the LaMnO-terminated $LaMnO_3$ surface models, MD simulations at 1073 K were carried out. In this study, only **Mn-c** and **Mn-c-V** intermediates on the perfect and defective $LaMnO_3$ surfaces, respectively, were used to generate a reactant gas-phase oxygen by elongating the distance between an O_2 molecule and the surface at approximately 4 Å. Then similar to the surface calculations, only the O_2 species and three top layers of the surface were fully relaxed. While the simulations were carried out using the NVT ensemble with the Nosé-Hoover thermostat,[67] the equations of motion were integrated using the Verlet algorithm[68] with a time step of 2 fs. The calculations were iterated until they reached an equilibrium state.

MD Simulations on the Perfect Surface at 1073 K. Figure 7a shows the snapshots of configurations calculated according to time evolution, representing the adsorption and dissociation of a triplet gas-phase oxygen molecule, while Figure 7b displays the change of the energy profile and O−O

(64) Wang, W.; Zhang, H.-b.; Lin, G.-d.; Xiong, Z.-t. *Appl. Catal. B* **2000**, *24*, 219.
(65) As Hehre and coworkers reported (see ref 66), a large number of comprehensive experimental values are needed to obtain reliable correction factors for estimated vibrational frequencies.
(66) Hehre, W. J.; Radom, L.; Schleyer, P. v. R.; Pople, J. A. *Ab initio molecular orbital theory*; John Wiley & Sons, Inc.: New York, 1986.
(67) Palmer, M. S.; Neurock, M.; Olken, M. M. *J. Am. Chem. Soc.* **2002**, *124*, 8452.
(68) Verlet, L. *Phys. Rev.* **1967**, *159*, 98.

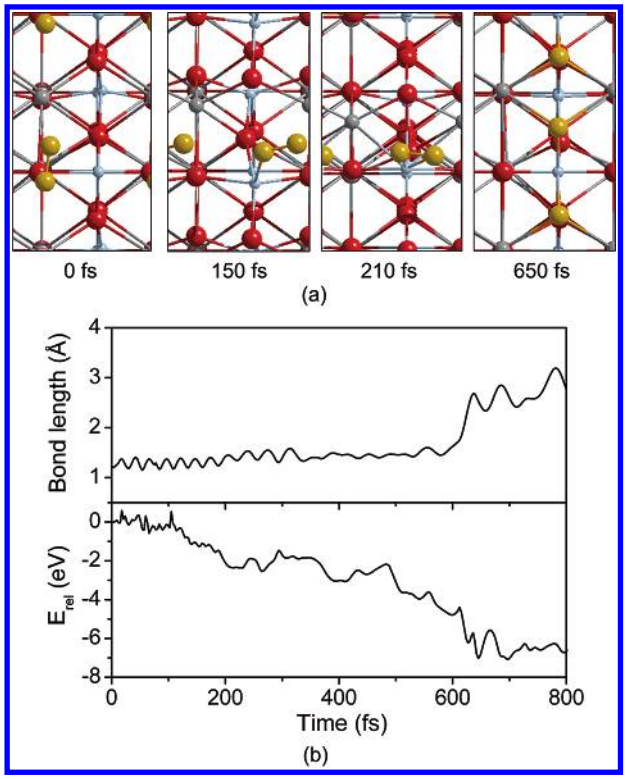

Figure 7. MD simulations for the oxygen reduction on the perfect $LaMnO_3$ surface at 1073 K. (a) Top views of configurations. (b) The variation of energetics and O−O distance.

distance. As the oxygen molecule moves toward the surface, the energies are initially oscillating with a small fluctuation of the O−O bond length. The bond distance of the reactant oxygen molecule is 1.241 Å, which is close to the predicted bond length of a triplet O_2 at 1.235 Å. We placed an oxygen molecule in a configuration similar to that of **Mn-c**; therefore, one of the oxygen atoms, **O1**, is slightly closer to the surface than **O2**. As time evolves, it rotates and becomes parallel to the surface as shown in Figure 7a. The initial energy barriers from 0 fs to ∼135 fs may result from thermal equilibration since we used the structures optimized at 0 K. The adsorption with a superoxo-like configuration occurs approximately in 150 fs. While its OO bond length of 1.785 Å is considerably longer than that of **Mn-c** (1.314 Å) optimized at 0 K (see Figure 3), the distance between **O1** and the surface is also not significantly longer. After the configuration change with a significant energy decrease, the superoxo-like species converts to a peroxo-like species in ∼60 fs with an energy difference of approximately 0.43 eV, which is in agreement with that estimated at 0 K (0.44 eV). Then, the peroxo-like species dissociates while diffusing on the surface. However, we found that the barrier at ∼670 fs is due to the surface diffusion of the adsorbed oxygen species, not due to the dissociation as we verified in the previous section using the NEB method. As displayed in Figure 5, the most stable di-oxygen configuration is the intermediate just before dissociation. All the processes from adsorption to dissociation may take place in 650 fs under SOFC operating conditions via this reaction pathway. On the basis of the MD modeling at 1073 K, the O_2 dissociation after adsorption at the perfect $LaMnO_3$ surface occurs in approximately 450 fs.

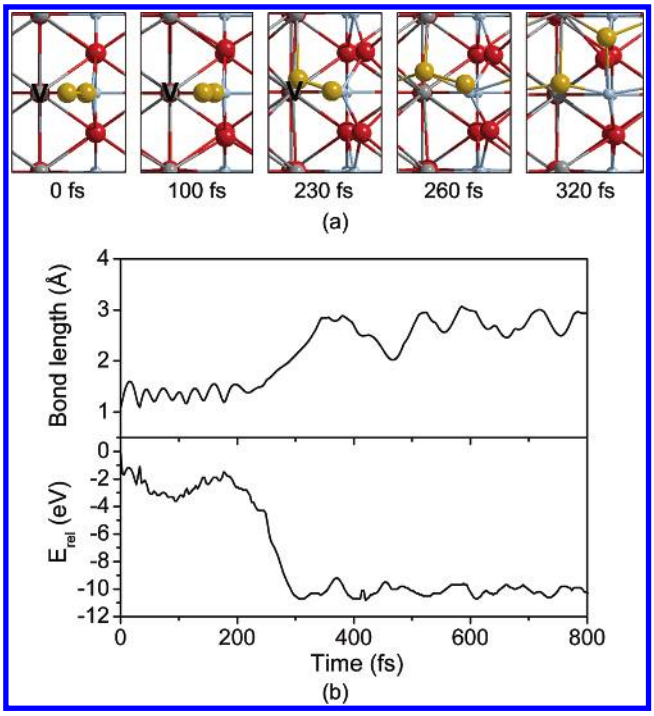

Figure 8. MD simulations for the oxygen reduction on the defective $LaMnO_3$ surface at 1073 K. (a) Top views of configurations. (b) The variation of energetics and O−O distance.

MD Simulations on the Defective Surface at 1073 K. As illustrated in Figure 8b, compared with the perfect $LaMnO_3$ surface, the dissociation kinetics become faster on the defective surface. As shown in Figure 8a, the molecular adsorption of a superoxo-like species occurs in 100 fs. Then, one of the oxygen atoms of the adsorbed species moves toward the oxygen vacancy with energy stabilization and charge transfer, which takes place in approximately 130 fs. After the incorporation process in an additional 30 fs, the adsorbed oxygen monatomic species at Mn cations diffuses to a more stable site at **O-II** (see Figures 2c and 4). The time from adsorption to dissociation (with incorporation) was 220 fs.

Even though the NEB calculations determined two pathways via superoxo- and peroxo-like species without a reaction barrier, the MD simulations with our surface models suggested that the most probable reaction pathway is the formation of superoxo-like species and then conversion to peroxo-like species with a small reaction barrier. Thus, we can write out two possible routes without (**I**) and with (**II**) oxygen vacancies on the $LaMnO_3$-based surfaces.[21] We summarize the most probable pathway for the oxygen-reduction mechanism based on the DFT/MD modeling in Scheme 1, where (g), (ads), (super), (per), and (lc) represent gas, molecular adsorption, superoxo-like species, peroxo-like species, and lattice, respectively.

E. Implications for Phenomenological Modeling. It may not be necessary to wait for the development of advanced surface characterization techniques to experimentally assess the DFT/MD results presented here. Instead, the likely mechanism can be incorporated into a phenomenological/continuum framework and assessed against macroscopic experiments such as electrochemical tests. Qualitatively, the most salient aspect of this work is the fact that the energy

Scheme 1. Mechanism of the Oxygen Reduction Reaction on the $LaMnO_3$ Cathode Materials[a]

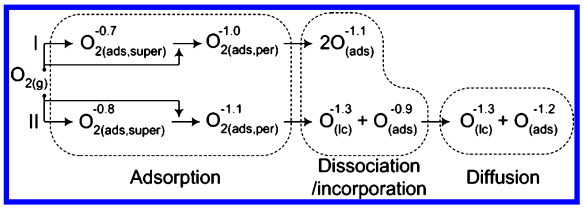

[a] The superscript values are the atomic charges in the unit of *e* estimated from the Bader analysis.[54,55]

barriers for all steps are low or nonexistant. MD simulations confirm the fast kinetics of the adsorption, dissociation, and incorporation steps. We can therefore expect that reaction rates will be dominated by the variational transition state of the adsorption process according to the variational transition-state theory (VTST) formalism.[69]

Our MD simulations show that the superoxo adsorbate has a very limited lifetime (60 fs) before becoming further reduced to the peroxo molecule. We may therefore write

$$O_2 + s \rightarrow O_2'' + 2h^{\bullet} \tag{2}$$

where O_2'' is the peroxo-like adsorbate, $h^{\bullet}$ is an electron hole, and *s* is an unoccupied surface adsorption site. It is also the case that dissociation from peroxo-like species to atomic oxygen is a fast process (450 fs); however, this reaction also involves an additional surface site. At the high coverage that we can expect at moderate oxygen pressures due to the high exothermicity of the adsorption and dissociation process, site availability may become low. Therefore, we must separately consider the dissociation reaction:

$$O_2'' + s \rightarrow 2O' \tag{3}$$

where O' is an adsorbed oxygen atom. As written, this does not seem to be a charge-transfer step; however, inasmuch as the location of the atomic charge with respect to the surface changes in the reaction, the surface potential will have some effect on (and be affected by) reaction 3.

Incorporation of oxygen in the presence of an oxygen vacancy is also a very fast process, for both atomic and molecular species, with the latter undergoing dissociation and adsorption in the presence of a vacancy in what is tantamount to a single step. The resulting rates are again dependent mostly on the availability of vacancies. The reactions may be written as

$$O_2'' + V_O^{\bullet\bullet} \rightarrow O_O^X + O' + h^{\bullet} \tag{4}$$

and

$$O' + V_O^{\bullet\bullet} \rightarrow O_O^X + h^{\bullet} \tag{5}$$

where O_O^X denotes a neutral oxygen ion in a solid-state oxygen site. All of these reactions are, phenomenologically, charge-transfer reactions between the material and the surface. As such, the nonequilibrium reaction rate equations must take into account the deviation of the surface potential $\Delta\chi$ from its equilibrium value.[70] For example, in the case of the adsorption reaction 2:

$$r_{ads} = k_{ads}{}^0 \left[\frac{1-\gamma}{1-\gamma_0} \exp\left(\frac{-\alpha F \Delta\chi}{RT}\right) - \frac{\theta c_h{}^2}{\theta_0 c_{h,0}{}^2} \exp\left(\frac{(1-\alpha) F \Delta\chi}{RT}\right) \right] \tag{6}$$

where γ is the total site coverage, c_h is the concentration of electron holes at the surface, θ is the site coverage of superoxo, α is the transfer coefficient, and the subscript 0 represents the equilibrium value. $k_{ads}{}^0$ is the exchange rate constant,

$$k_{ads}{}^0 = \vec{k}_{ads} P_{O_2} \Gamma (1-\gamma_0) = \overleftarrow{k}_{ads} \Gamma \theta_0 c_{h,0}{}^2 \tag{7}$$

where Γ, $\vec{k}_{ads}$, and $\overleftarrow{k}_{ads}$ are the total concentration of surface sites and forward and reverse rate constants, respectively.

In a continuum model, $\Delta\chi$ is calculated by relating charge densities, calculated in terms of atomic charge through first-principles calculations, to potential through Poisson's equation. The forward and reverse rate constants for this reaction can be calculated by using the VTST formalism.[69] However, detailed rate-constant predictions based on the potential energy profiles are not straightforward because an enormous amount of computational time is needed to map out the variational transition state along the MEPs.

Given the high equilibrium constants for adsorption and non-vacancy-mediated dissociation, it is likely that the surface coverage on the LSM surface will be large, consisting mostly of atomic oxygen. Such a situation should lead to reconsideration of the Langmuir isotherm typically employed in phenomenological modeling of LSM,[71−75] perhaps in favor of a new model which accounts, in some way, for lateral adsorbate interaction. It is this interaction model, along with a consideration of site statistics that are distinct for each crystal face, which may lead to a particular form of the rate equations for reactions 2−5.

4. Conclusion

O_2−$LaMnO_3$ interactions were predicted using periodic DFT/MD calculations. It was found that the oxygen reduction can occur via molecular and dissociative adsorption. Surface species on La, Mn, and O_{sub} sites were identified at 0 K as superoxo- or peroxo-like species based on their estimated geometries and vibrational modes (O−O stretching bands at 1143−1265 or 861−979 cm^{-1}, respectively), depending on configurations. However, the whole process occurred with small reaction barriers or without barrier at both perfect and defective $LaMnO_3$ surfaces, suggesting fast kinetics for oxygen reduction on the surfaces. It was also found that

(69) Laidler, K. J. *Chemical Kinetics*, 3rd ed.; Harper and Row: New York, 1987.
(70) Mebane, D. S.; Liu, M. *J. Solid State Electrochem.* **2006**, *10*, 575.
(71) Adler, S. B.; Lane, J. A.; Steele, B. C. H. *J. Electrochem. Soc.* **1996**, *143*, 3554.
(72) Svensson, A. M.; Sunde, S.; Nisancioglu, K. *J. Electrochem. Soc.* **1997**, *144*, 2719.
(73) Coffey, G. W.; Pederson, L. R.; Rieke, P. C. *J. Electrochem. Soc.* **2003**, *150*, A1139.
(74) Williford, R. E.; Singh, P. *J. Power Sources* **2004**, *128*, 45.
(75) Mebane, D. S.; Liu, Y.; Liu, M. L. *J. Electrochem. Soc.* **2007**, in press.

oxygen vacancies influence the oxygen reduction kinetics. The O_2 adsorption of **La-a-v** is less strong than that of **Mn-c** (−1.51 vs −1.76 eV, respectively), tentatively showing that B cation sites are more active toward oxygen reduction. However, to verify the experimental observations,[21] a comparative computational study of different B cations has to be carried out. More accurate prediction of reaction barriers and molecular parameters for kinetic studies may be possible using the GGA + U approach reported by Wang and co-workers,[76] in which more reliable oxidation energies of various transition metal oxides were predicted. The oxygen-vacancy formation energy of $LaMnO_3$ will therefore also be evaluated using the GGA + U method[76] in a future study. In addition, it may be desirable to examine the reaction on orthorhombic $LaMnO_3$ (*Pnma*) to estimate how the Jahn−Teller distortion may affect oxygen reduction. The DFT/MD modeling is useful for elucidating the oxygen reduction mechanism at the SOFC cathode surfaces; these and similar results for other electrode materials may aid in the development of more efficient and cheaper electrodes. On the basis of our conclusions, it is possible to develop a continuum framework that includes the prediction of atomic charges of each possible species and product, which will be applied in subsequent macroscopic modeling. To fully understand the oxygen reduction reaction under the SOFC conditions, further in situ spectroscopic and theoretical investigations will be explored.

Acknowledgment. We are grateful for the financial support provided by DOE-NETL University Coal Program (Grant DE-FG26-06NT42735) and DOE Basic Energy Science (Grant DE-FG02-06ER15837). The authors acknowledge the use of CPUs from National Center for High-performance Computing, Taiwan, supported by INER under Contract No. NL 940251. M.C.L. also wants to acknowledge support from the MOE ATP program, Taiwan Semiconductor Manufacturing Co., for the TSMC Distinguished Professorship and Taiwan National Science Council for the Distinguished Visiting Professorship at the Center for Interdisciplinary Molecular Science, National Chiao Tung University, Hsinchu, Taiwan. We appreciate the reviewers' valuable comments which made the manuscript more informative.

Supporting Information Available: Figure S1 illustrates the (111) and (110) surfaces used for surface stability calculations and a summary of the results. Figure S2 shows the partial density of states of Mn ions on the cubic $LaMnO_3$ surface. The properties of predicted gas-phase triplet and singlet oxygen species are compiled in Table S1. Tables S2 and S3 give the atomic charges for the bulk and surface calculations (PDF). This material is available free of charge via the Internet at http://pubs.acs.org.

CM062616E

(76) Wang, L.; Maxisch, T.; Ceder, G. *Phys. Rev. B* **2006**, *73*, 195107/1.